Nano Research Energy

ISSN 2791-0091 (print); 2790-8119 (online)
https://doi.org/10.26599/NRE.2026.9120233

Research Article

Building interfacial kinetic pathways via reverse hydrogen spillover to accelerate alkaline hydrogen evolution reaction

Guangxin Ren[1,§], Aixian Shan[1,2,§] (✉), Kaibin Su[1], Yuqing Xu[1], Yingying Xu[1] (✉), and Rongming Wang[1] (✉)

[1] *The State Key Laboratory for Advanced Metals and Materials, School of Mathematics and Physics, Beijing Key Laboratory for Magneto-Photoelectrical Composite and Interface Science, University of Science and Technology Beijing, Beijing* 100083, *China*
[2] *Department of Chemical and Materials Engineering, The University of Auckland, Auckland* 1142, *New Zealand*
[§] *Guangxin Ren and Aixian Shan contributed equally to this work.*

Received: 23 February 2026 / **Revised:** 8 April 2026 / **Accepted:** 10 April 2026 / **Published date:** 15 May 2026

ABSTRACT

Dual-active-site strategies are widely adopted to address the intrinsic challenge of simultaneously promoting water dissociation and maintaining an optimal hydrogen adsorption free energy in alkaline hydrogen evolution. However, this paradigm implicitly presumes rapid equilibration of hydrogen intermediates (H*), thereby neglecting H* transport as a fundamental kinetic bottleneck. Here, we show that rational regulation of interfacial hydrogen-spillover pathways offers an effective kinetic lever for modulating alkaline hydrogen evolution. An atomically coupled Pt-Co_3O_4 heterostructure, featuring Pt nanoparticles anchored on Co_3O_4 nanowire arrays, is constructed as a model system. We reveal that interfacial electron transfer generates a built-in electric field, which can be effectively tuned via oxygen-vacancy-mediated modulation of the work function difference, thereby enabling controllable regulation of interfacial H* migration. This field drives a reverse hydrogen spillover process and lowers the H* migration barrier to 0.13 eV, transforming the heterointerface into a high-efficiency H* transport channel. Enabled by this field-regulated reaction pathway, the catalyst delivers an overpotential of 18.7 mV at 10 mA·cm^{-2} and a Tafel slope of 27.8 mV·dec^{-1} in 1.0 M KOH. The practical relevance is validated by alkaline seawater electrolysis, delivering 1.0 A·cm^{-2} at 1.76 V and maintaining stable performance for over 500 h. This research clarifies the electronic origin of accelerated reverse hydrogen spillover and offers a universal design paradigm for high-performance multi-step electrocatalysis.

KEYWORDS

Pt-Co_3O_4 heterostructures, reverse hydrogen spillover, built-in electric field, alkaline hydrogen evolution reaction, seawater electrolysis

1 Instruction

Hydrogen energy has attracted substantial attention as a high-density, zero-emission energy carrier [1, 2]. Among various hydrogen production technologies, alkaline water electrolysis stands out for its technological maturity and high operational safety [3–6]. In particular, alkaline seawater electrolysis offers a scalable pathway by leveraging abundant natural resources while effectively suppressing the competing chlorine evolution reaction under high-pH conditions [7, 8]. However, the hydrogen evolution reaction (HER) in alkaline media suffers from intrinsically sluggish kinetics due to the additional water dissociation step, imposing a critical demand for catalysts capable of simultaneously accelerating water activation and hydrogen adsorption/desorption at industrial current densities [9–12].

Platinum (Pt)-based catalysts occupy the peak of the HER volcano plot owing to their near-optimal hydrogen adsorption energy (ΔG_{H^*}) [13]. However, in alkaline environments, even Pt kinetically hindered by limited water dissociation capability [14]. To overcome this limitation, recent research efforts have shifted from single-site optimization to interfacial catalyst design, leveraging support materials with high hydrolytic activity in conjunction with Pt to construct dual active sites that enable the redistribution of reaction steps across distinct components [15–19]. Such heterostructure catalysts generally outperform their single-component counterparts in alkaline HER, highlighting the importance of interfacial coupling.

Despite considerable progress in such heterostructure catalysts, the majority of studies implicitly assume rapid equilibration of H* between the two active sites. Under this assumption, interfacial H* migration is not treated as an independent, kinetically relevant elementary step, and catalytic performance is still predominantly rationalized using static electronic descriptors, such as ΔG_{H^*} or water dissociation barriers. In fact, such interfacial H* migration is extremely crucial and has a clear physical analogue, namely

© The Author(s) 2026. Published by Tsinghua University Press. The articles published in this open access journal are distributed under the terms of the Creative Commons Attribution 4.0 International License (http://creativecommons.org/licenses/by/4.0/), which permits use, distribution and reproduction in any medium, provided the original work is properly cited.

Address correspondence to Aixian Shan, axshan@ustb.edu.cn; Yingying Xu, xuyingying@ustb.edu.cn; Rongming Wang, rmwang@ustb.edu.cn

hydrogen spillover. In thermocatalytic systems, hydrogen spillover is widely recognized as a key interfacial process involving the migration of activated hydrogen species from metal surfaces to adjacent supports [20, 21]. By analogy, the concept of hydrogen spillover has recently been extended to electrocatalytic hydrogen evolution to rationalize and enhance interfacial activity [22, 23]. For example, Yao et al. constructed a PtCo@La-TiO_2 heterostructure that boosts the HER performance by leveraging an enhanced hydrogen spillover effect [24]. Similarly, Ma et al. tuned the work function difference between the metal and the support to reduce the interfacial hydrogen migration barrier, enabling efficient hydrogen spillover. The resulting Pt_2Ir_1/CoP catalyst also exhibited outstanding HER performance [25].

However, under alkaline conditions, particularly in catalytic systems incorporating strongly hydrophilic oxide supports, water molecules preferentially adsorb and dissociate on the oxide surface, such that H* are more likely to form initially on the support rather than on metal sites [15]. The subsequent transfer of these H* species to adjacent metal sites, namely reverse hydrogen spillover, is not necessarily spontaneous or rapid, and may involve a substantial energy barrier, rendering it a potentially critical process governing the overall kinetics of hydrogen evolution. Its microscopic driving force, quantitative kinetic barrier, and potential role as the rate-determining step are not clearly established, lacking direct experimental validation and a detailed electronic-structure-level understanding. Moreover, how to rationally construct a catalyst interface with a high-speed reverse spillover channel remains an unresolved challenge, hindering the targeted optimization of alkaline HER kinetics.

We propose that constructing a built-in interfacial electric field (BEF) to catalyze directional "reverse hydrogen spillover" is the key to kinetically coupling water dissociation and hydrogen evolution for Pt-transition metal oxide heterostructures. We select cobalt oxide (Co_3O_4) as the ideal partner for Pt. Co_3O_4 has attracted particular interest due to its mixed-valence Co^{2+}/Co^{3+} states, strong water affinity, and intrinsic ability to facilitate hydroxyl adsorption and O-H bond cleavage [26, 27]. Such Pt-Co_3O_4 catalysts have been demonstrated to exhibit markedly enhanced alkaline HER performance compared with their single-component counterparts [28]. In such a heterostructure, the difference in work function between Pt (~5.7 eV) and Co_3O_4 (~5.0 eV) is expected to induce interfacial electron transfer upon contact, potentially leading to the formation of a BEF. This interfacial field may influence the transport behavior of H* via spillover. Meanwhile, the work function of Co_3O_4 can be modulated by tuning its oxygen vacancy concentration, which may provide a feasible platform for regulating the interfacial electric field and exploring its potential role in H* migration kinetics.

To validate this hypothesis and harness this predicted effect, we realize a high-speed interfacial reverse hydrogen spillover pathway in an atomically coupled Pt-Co_3O_4 heterostructure, establishing an integrated dissociation-migration-desorption catalytic system that overcomes kinetic bottlenecks in alkaline HER. Combining systematic electrochemical measurements, *operando* spectroscopic analyses, and DFT theoretical calculations, we directly identify this reverse hydrogen spillover process and elucidate its role in promoting interfacial reaction kinetics during alkaline HER. More importantly, we reveal that interfacial electronic coupling induces a BEF that significantly lowers the energy barrier for reverse hydrogen spillover, thereby transforming the interface into an efficient hydrogen-transport channel. Benefiting from this interface-engineered mechanism, the Pt-Co_3O_4/CC catalyst achieves 10 mA·cm^{-2} at an overpotential of only 18.7 mV in 1.0 M KOH and demonstrates industrial-level seawater electrolysis performance (1.0 A·cm^{-2} at 1.76 V) with long-term stability. Our study provides direct mechanistic insights and design principles for the development of high-performance HER catalysts.

2 Result and discussion

2.1 Catalyst synthesis and structural characterization

The carbon cloth-supported Pt-Co_3O_4 porous nanowire electrocatalysts were rationally designed and fabricated to generate abundant heterointerfaces through intimate interfacial contact enabled by an *in situ* growth strategy. Specifically, Co_3O_4 porous nanowires were first grown on carbon cloth (CC) via a hydrothermal process followed by air calcination. Pt nanoparticles (NPs) were then uniformly deposited onto the nanowires through electrodeposition, yielding the final Pt-Co_3O_4/CC heterostructures catalysts (Fig. 1(a)). X-ray powder diffraction (XRD) analysis confirms the successful synthesis of Co_3O_4, while the absence of characteristic Pt peaks in the Pt-Co_3O_4/CC pattern suggests a low Pt loading with high dispersion on the Co_3O_4 substrate (Fig. 1(b)). Consistently, Raman spectra indicates that the Co_3O_4 phase remains intact after electrodeposition (Fig. S1 in the Electronic Supplementary Material (ESM)) [29, 30]. Scanning electron microscopy (SEM) images show a well-preserved, spatially interwoven nanowire array architecture throughout the synthesis (Fig. 1(c) and Fig. S2 in the ESM), which is conducive to uniform metal dispersion and efficient mass transport. Notably, transmission electron microscopy (TEM) analysis of the Co_3O_4 and Pt-Co_3O_4 nanowires reveals a particle-assembled structure with abundant hierarchical porosity (Figs. S3 and S4 in the ESM and Fig. 1(e)), which maximizes active-site exposure. The favorable interfacial properties are further corroborated by surface wettability measurements. Both Co_3O_4/CC and Pt-Co_3O_4/CC exhibit superhydrophilicity (contact angle ~ 0°), contrasting sharply with the hydrophobic pristine carbon cloth (103.9°) (Fig. 1(d)), thereby ensuring rapid electrolyte infiltration and full accessibility to the active sites [31, 32].

High-angle annular dark-field scanning transmission electron microscopy (HAADF-STEM) clearly reveals Pt nanoparticles uniformly anchored on the Co_3O_4 nanowires, with an average particle size of approximately 20.4 nm (Figs. S5(a) and S5(b) in the ESM). Elemental mapping and corresponding EDX spectra further verify the homogeneous spatial distribution of Pt, confirming the formation of well-defined Pt-Co_3O_4 heterointerfaces across the nanowire surface (Figs. S5(c)–S5(g)) in the ESM). Such a uniform interfacial configuration ensures extensive metal-oxide contact, which is critical for efficient interfacial charge transfer and synergistic catalytic functionality (Fig. S6 in the ESM). To further elucidate the heterointerface structure of Pt-Co_3O_4 at the atomic scale. HAADF-STEM imaging was used to precisely locate the interface region. As shown in Fig. 1(f), Pt NPs are clearly anchored on the surface of Co_3O_4, enabling direct identification of the heterostructure interface. Subsequent HRTEM analysis of this region identifies two distinct crystalline domains within the heterostructure (Fig. 1(g)). In the Co_3O_4 domain, a uniform lattice spacing of 0.286 nm is observed in all directions, while the corresponding fast Fourier transform (FFT) pattern exhibits sixfold symmetry (Fig. 1(h) and Fig. S7(a) in the ESM). These features indicate that the Co_3O_4 domain is

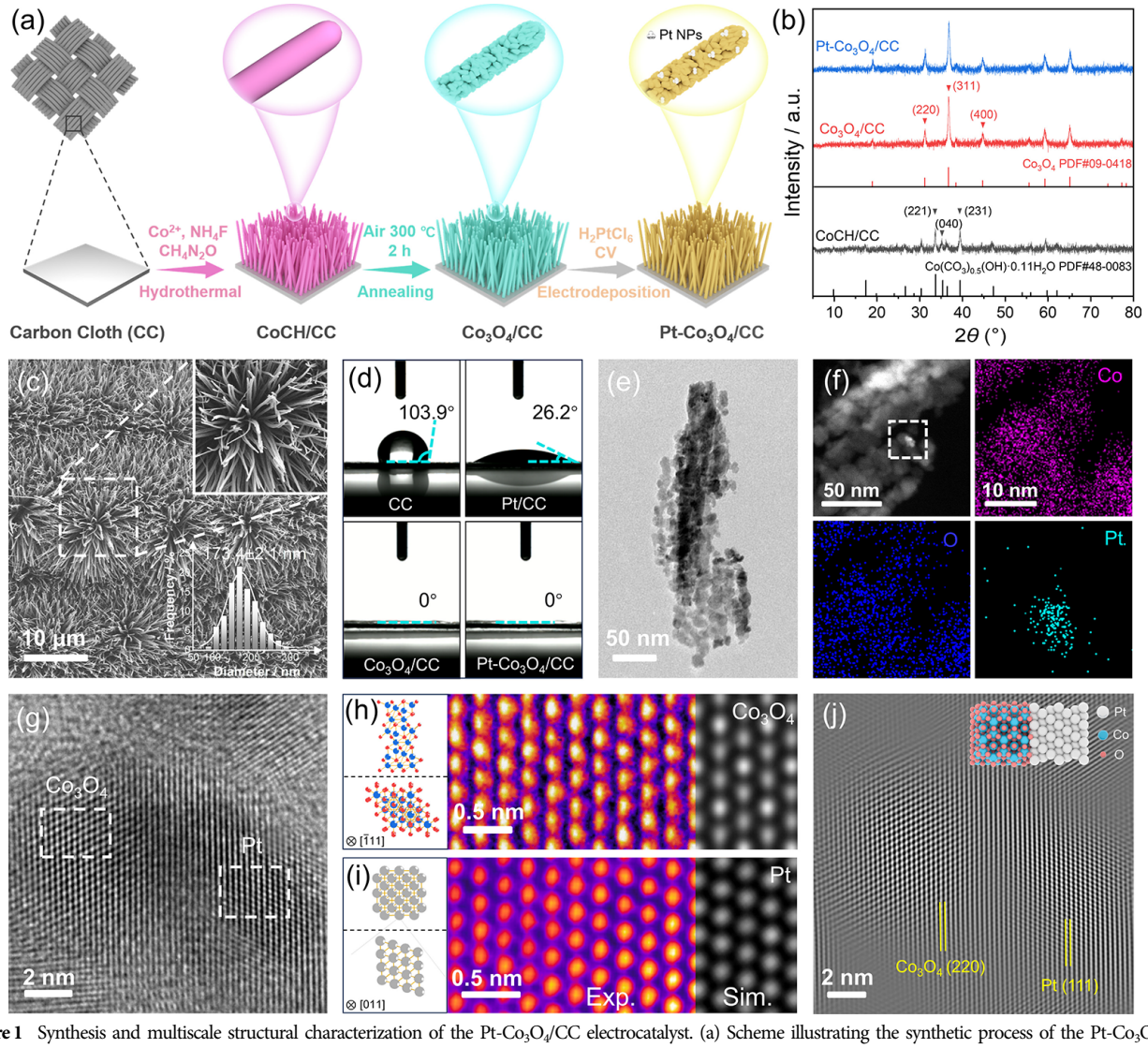

Figure 1 Synthesis and multiscale structural characterization of the Pt-Co_3O_4/CC electrocatalyst. (a) Scheme illustrating the synthetic process of the Pt-Co_3O_4/CC electrocatalyst. (b) XRD patterns of CoCH/CC, Co_3O_4/CC, and Pt-Co_3O_4/CC. (c) SEM images of Pt-Co_3O_4/CC with the inset showing the diameter distribution of Co_3O_4 nanowires. (d) Static contact angles of CC, Pt/CC, Co_3O_4/CC, and Pt-Co_3O_4/CC. (e) TEM image of Pt-Co_3O_4. (f) HAADF-STEM image and corresponding elemental mappings of Co, O, and Pt for Pt-Co_3O_4. (g) HRTEM images of Pt-Co_3O_4/CC. (h, i) (From left to right) Structural model of the fundamental repeat unit of Co_3O_4 viewed along the [$\bar{1}$11] zone axis for Co_3O_4 (h) and structural model viewed along the [0 1 1] zone axis for Pt (i); an enlarged HRTEM image of Co_3O_4 (h) and Pt (i); and the corresponding QSTEM-simulated HRTEM image based on the structural model. (j) Inverse Fourier transform image of the heterostructure formed between the Co_3O_4 (220) and Pt (111) planes, illustrated with a proposed atomic structure model, with blue, pink and white spheres representing Co, O, and Pt atoms, respectively.

oriented along the [$\bar{1}$11] zone axis, with the measured lattice planes indexed to the {220} family. By contrast, the Pt domain is oriented along the [011] zone axis, as evidenced by lattice spacings of 0.226 and 0.196 nm corresponding to the {111} and {200} families of face-centered cubic Pt, respectively (Fig. 1(i) and Fig. S7(b) in the ESM). To validate the TEM results and better understand the crystal structure, an atomic model was constructed from the measured lattice spacings, interplanar angles, and crystallographic orientations, with HRTEM simulations performed using QSTEM software (Figs. 1(h) and 1(i)) [33]. A remarkable agreement is observed between the experimental HRTEM images and the QSTEM simulations, both in atomic arrangement and interplanar spacing. This consistency unambiguously validates the high crystallinity and predetermined crystallographic orientation of the as-synthesized Co_3O_4 and Pt nanocrystals. Building upon the confirmed individual phases, we examined the Co_3O_4/Pt interface. The inverse Fourier transform filtered image of the heterostructure alongside a proposed atomic structure (Fig. 1(j)) reveals an atomically sharp contact between the Co_3O_4 (220) and Pt (111) planes. This preferential alignment indicates a low lattice mismatch between these facets, effectively reducing the interfacial energy and favoring its stabilization. In summary, Pt/Co_3O_4 heterostructures with well-defined atomic interfaces were uniformly constructed on porous Co_3O_4 nanowires grown *in situ* on carbon cloth, as confirmed by atomic-resolution TEM and image simulations.

2.2 Surface elemental composition and chemical state

The surface elemental composition and chemical states of the sample were analyzed using X-ray photoelectron spectroscopy (XPS). The survey spectrum confirms the presence of Pt, Co, and O in Pt-Co_3O_4/CC (Fig. S8 in the ESM). High-resolution Pt 4f spectra of Pt-Co_3O_4/CC display two spin-orbit doublets corresponding to Pt^0 and Pt^{2+} species (Fig. 2(a)). Specifically, the

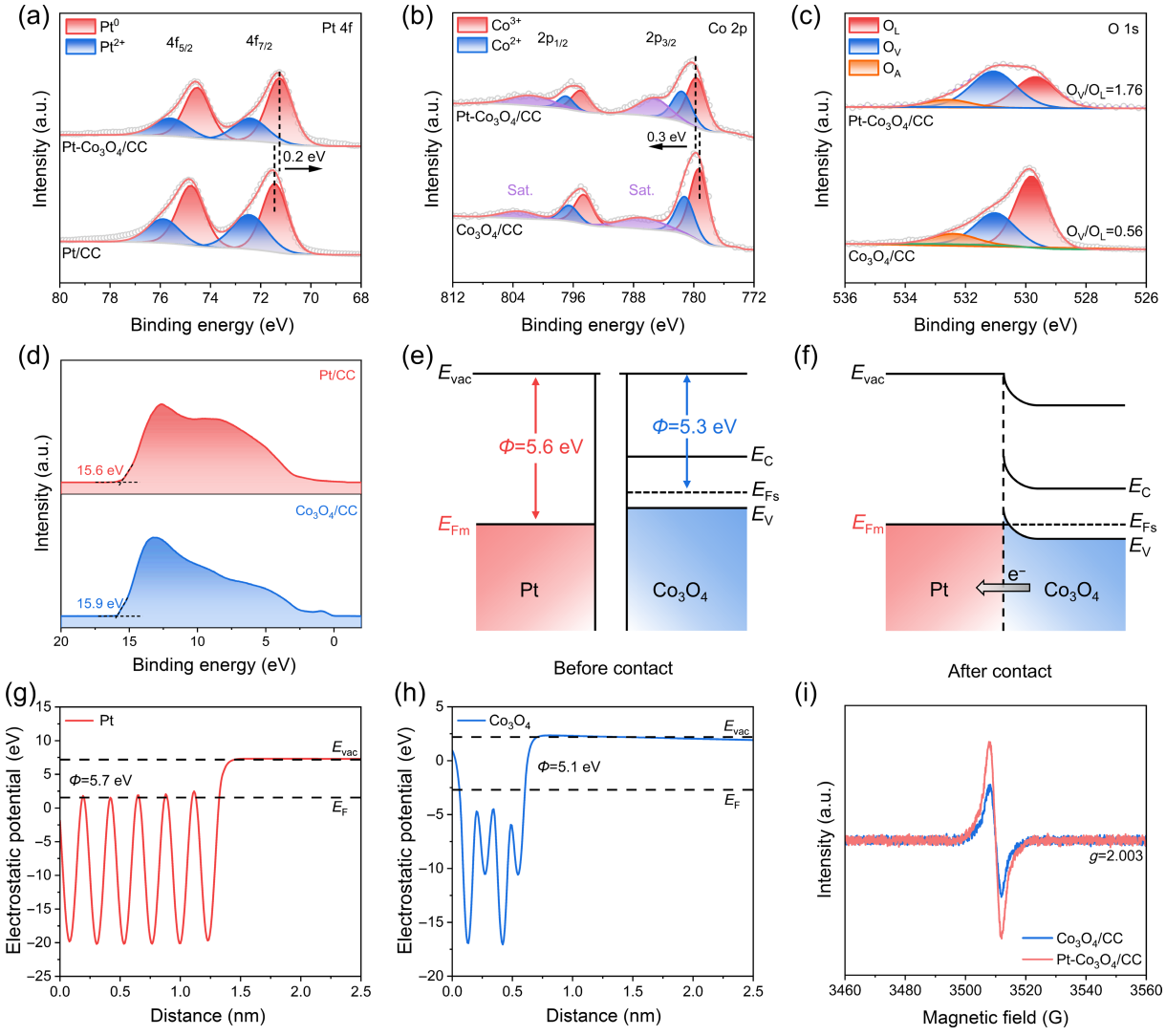

Figure 2 Electronic structure characterization and interfacial charge redistribution in the Pt-Co_3O_4 heterostructure. High-resolution XPS spectra of (a) Pt 4f for Pt/CC and Pt-Co_3O_4/CC, (b) Co 2p for Co_3O_4/CC and Pt-Co_3O_4/CC, and (c) O 1s for Co_3O_4/CC and Pt-Co_3O_4/CC. (d) UPS spectra of Pt/CC and Co_3O_4/CC. Energy band diagrams of the Pt and Co_3O_4 phases before (e) and after (f) contact. Work function of (g) Pt and (h) Co_3O_4. (i) EPR spectra of Co_3O_4/CC and Pt-Co_3O_4/CC.

peaks at 71.2 and 74.5 eV are assigned to metallic Pt^0, while those at 72.3 and 75.6 eV are indicative of Pt^{2+} species [34]. Compared to Pt/CC, the Pt 4f peaks in Pt-Co_3O_4/CC exhibit a slight negative shift of 0.2 eV, suggesting an electron-rich environment at the Pt sites. The Co 2p spectra of Pt-Co_3O_4/CC can be deconvoluted into Co^{3+} (779.6/795.0 eV), Co^{2+} (781.5/797.0 eV), and characteristic satellite peaks (Fig. 2(b)) [35]. Relative to pristine Co_3O_4, the Co 2p peaks exhibit a positive shift of 0.3 eV, indicating an electron-deficient environment at the Co sites. The opposite binding energy shifts of Pt and Co unambiguously evidence interfacial charge redistribution, reflecting electron transfer from Co_3O_4 to Pt and resulting in the formation of a BEF at the interface [36]. In the O 1s spectra of both Co_3O_4/CC and Pt-Co_3O_4/CC, the peaks located at 529.6, 531.1, and 532.6 eV are assigned to lattice oxygen (O_L), oxygen vacancies (O_V), and surface-adsorbed oxygen species (O_A), respectively (Fig. 2(c)) [37]. The O_V concentration, quantified by the O_V/O_L ratio, is significantly higher for Pt-Co_3O_4/CC (1.76) than for Co_3O_4/CC (0.56), indicating that Pt loading promotes the formation of O_V [38]. Ultraviolet photoelectron spectroscopy (UPS) was employed to probe the work functions (Φ) of Pt/CC and Co_3O_4/CC, providing insight into the interfacial electronic modulation in Pt-Co_3O_4/CC (Fig. 2(d)) [39, 40]. The measured Φ values are 5.6 eV for Pt and 5.3 eV for Co_3O_4 ($\Phi = h\nu - |E_{cutoff} - E_F|$), indicating a tendency for electrons to flow from Co_3O_4 to Pt at the interface (Figs. 2(e) and 2(f)). Additionally, theoretical calculations predict work functions of 5.7 eV for Pt and 5.1 eV for Co_3O_4 (Figs. 2(g) and 2(h)), consistent with the experimental XPS and UPS results, thereby corroborating interfacial charge redistribution and the formation of a BEF across the heterointerface. The signal at g = 2.003 in the electron paramagnetic resonance (EPR) spectra was employed to evaluate the concentration of oxygen vacancies in the samples [41]. Notably, Pt-Co_3O_4/CC exhibits a significantly stronger EPR signal associated with O_V compared to Co_3O_4/CC, consistent with the increased O_V concentration revealed by O 1s XPS analysis (Fig. 2(i)). These abundant O_V promote interfacial water adsorption and facilitate O-H bond cleavage, thereby accelerating proton generation and facilitating the Volmer step in HER [42]. To further elucidate the role of oxygen vacancies in modulating the electronic structure, a series of Co_3O_4 supports with different oxygen vacancy concentrations were prepared by varying the oxygen partial pressure during synthesis, followed by Pt deposition to obtain the corresponding Pt-Co_3O_4 catalysts. XPS analysis shows that, as the oxygen partial pressure increases, the O_V/O_L

ratio of Co_3O_4 decreases from 1.01 in pure N_2 to 0.29 in pure O_2 (0.56 in air and 0.41 in a 1:1 N_2/O_2 mixture), indicating a progressive reduction in oxygen vacancy concentration (Fig. S9(a) in the ESM). After Pt deposition, although the overall oxygen vacancy concentration is significantly increased, the variation trend remains consistent with that of the pristine supports, with O_V/O_L ratios of 3.28, 1.76, 0.64, and 0.38, respectively (Fig. S9(b) in the ESM). UPS measurements further reveal that the work function of Co_3O_4 decreases as the oxygen vacancy concentration is reduced, thereby reducing the work function difference between Co_3O_4 and Pt and consequently modulating the strength of the interfacial BEF (Fig. S10 in the ESM).

2.3 Electrocatalytic HER performances

The HER performance of the as-prepared electrocatalysts was evaluated in a three-electrode system using 1.0 M KOH solution saturated with nitrogen. To optimize catalytic performance, electrocatalysts synthesized under varying experimental conditions (refer to the experimental section for details) were systematically assessed through linear sweep voltammetry (LSV). Initially, the concentration of the Pt precursor in the electrodeposition solution was tuned. As shown in Fig. S11 in the ESM, the catalyst prepared with 2.0 mM H_2PtCl_6 exhibits superior HER activity compared to other formulations. Subsequently, the influence of oxygen vacancy concentration on HER performance was systematically evaluated (Fig. S12 in the ESM). The HER activity shows a volcano-type dependence on oxygen vacancy concentration, increasing first and then decreasing. The Pt-Co_3O_4/CC catalyst obtained by calcination in air exhibits the optimal HER performance, suggesting that an appropriate oxygen vacancy concentration plays a critical role in modulating the interfacial electronic structure and HER kinetics. The optimized Pt-Co_3O_4/CC achieves current densities of 10 and 100 mA·cm^{-2} at overpotentials of 18.7 and 69.6 mV, respectively. These values are substantially lower than those observed of Pt/CC (44.9, 122.7 mV), Co_3O_4/CC (288.1, 346.1 mV), and commercial 20 wt.% Pt/C/CP (20.5, 81.6 mV) under identical experimental conditions (Figs. 3(a) and 3(b)). The Tafel slope extracted from the polarization curves provides key insight into the intrinsic kinetics of electrocatalytic HER. Pt-Co_3O_4/CC exhibits a remarkably low Tafel slope of 27.8 mV·dec^{-1}, substantially smaller than those of Pt/CC (51.5 mV·dec^{-1}), Co_3O_4/CC (119.4 mV·dec^{-1}), and even commercial 20 wt.% Pt/C/CP (30.1 mV·dec^{-1}), indicative of markedly accelerated HER kinetics (Fig. 3(c)). For conventional single-component catalysts, HER generally follows a Volmer-Heyrovsky or Volmer-Tafel mechanism, where Tafel slopes of ~120, ~40, and ~30 mV·dec^{-1} correspond to Volmer-, Heyrovsky-, and Tafel-limited kinetics, respectively. Accordingly, the rate-determining step (RDS) for Co_3O_4/CC, Pt/CC, and commercial wt.% Pt/C/CP can be assigned to the Volmer, Heyrovsky, and Tafel steps. Notably, the Tafel slope of Pt-Co_3O_4/CC (27.8 mV·dec^{-1}) is lower than that expected for a Tafel-step-limited mechanism, indicating a deviation from conventional HER kinetics. In light of previous reports linking hydrogen spillover to characteristic Tafel slopes of ~24 mV·dec^{-1}, this anomalous kinetic behavior suggests the possible involvement of hydrogen spillover in the HER process [43, 44]. The exchange current density (j_0), derived from the Tafel slope, is widely regarded as a quantitative descriptor of the intrinsic HER activity [45]. As illustrated in Fig. S13 in the ESM, the j_0 value for Pt-Co_3O_4/CC is 2.2 mA·cm^{-2}, which is 5.2 times higher than that of Pt/CC (0.42 mA·cm^{-2}), 20.0 times higher than Co_3O_4/CC (0.11 mA·cm^{-2}), and twice that of the commercial 20 wt.% Pt/C/CP (1.2 mA·cm^{-2}) catalyst, further emphasizing the superior HER activity of Pt-Co_3O_4/CC. To further assess catalytic efficiency, the specific mass activities of the Pt-Co_3O_4/CC and commercial 20 wt.% Pt/C/CP were calculated. The total mass of the Pt-Co_3O_4 electrocatalyst supported on carbon cloth was measured using a precision electronic balance (Fig. S14 in the ESM), while the platinum content in Pt-Co_3O_4 was quantified by inductively coupled plasma atomic emission spectroscopy (Table S1 in the ESM). After normalizing with respect to platinum loading, the mass activity of Pt-Co_3O_4/CC reaches 2.30 A·mg_{Pt}^{-1} at an overpotential of 100 mV, approximately 6.6 times higher than that of commercial Pt/C/CP (0.35 A·mg_{Pt}^{-1}), demonstrating significantly enhanced Pt utilization in Pt-Co_3O_4/CC (Fig. S15 in the ESM). The electrochemical impedance spectroscopy (EIS) data presented in Fig. 3(d) indicate that Pt-Co_3O_4/CC exhibits a substantially lower charge transfer resistance (R_{ct}) of 5.9 Ω compared to Pt/CC (48.5 Ω) and Co_3O_4/CC (167.6 Ω), indicating more efficient interfacial charge transfer and faster HER kinetics. The electrochemical surface area (ECSA), a critical parameter assessing accessible active sites and intrinsic catalytic activity, was estimated from the double-layer capacitance (C_{dl}) obtained through cyclic voltammetry (CV) measurements at various scan rates. The C_{dl} values for Pt/CC, Co_3O_4/CC, and Pt-Co_3O_4/CC are determined to be 31.6, 5.1, and 111.3 mF·cm^{-2}, respectively. This indicates that Pt-Co_3O_4/CC possesses the largest ECSA, thereby exposing a greater number of active sites compared to the other electrocatalysts (Fig. 3(e), Fig. S16 in the ESM). The intrinsic activity of electrocatalysts can also be evaluated by calculating the turnover frequency (TOF). As shown in Fig. 3(f), the TOF values for Pt-Co_3O_4/CC at overpotentials of 50 and 100 mV are 0.373 and 1.684 s^{-1}, respectively, which are substantially higher than those for Pt/CC (0.185, 0.816 s^{-1}) and Co_3O_4/CC (0.031, 0.069 s^{-1}) (Fig. S17 in the ESM). Based on the above findings, a radar chart was created to visually highlight the enhanced alkaline HER performance of Pt-Co_3O_4/CC in comparison with the reference catalysts (Fig. 3(g)). Furthermore, compared to most previously reported Pt-based catalysts, Pt-Co_3O_4/CC demonstrates favorable HER performance (Fig. 3(h), Table S2 in the ESM). The polarization curves of Pt-Co_3O_4/CC remain nearly unchanged before and after 5000 CV cycles (Fig. S18 in the ESM), indicating excellent electrochemical durability. Furthermore, chronopotentiometry measurements reveal that after more than 550 hours of operation, the overpotential of Pt-Co_3O_4/CC increases by only 5 mV, while the commercial 20 wt.% Pt/C/CP shows a 28 mV increase after 50 hours, underscoring the exceptional long-term stability of Pt-Co_3O_4/CC (Fig. 3(i)). To evaluate its structural and chemical integrity after prolonged testing, the Pt-Co_3O_4/CC catalyst was subjected to comprehensive post-stability characterization using XRD, Raman spectroscopy, XPS, and TEM. The XRD and Raman results confirm the preservation of the Co_3O_4 crystalline phase (Fig. S19 in the ESM), while HRTEM images show that the Pt/Co_3O_4 heterointerface remains intact (Fig. S20 in the ESM). Moreover, the XPS spectra obtained from the post-reaction sample exhibit a high degree of similarity to those of the fresh sample, indicating that the surface elemental states were largely preserved during the reaction process (Fig. S21 in the ESM).

2.4 Reverse hydrogen spillover mechanism

To further elucidate the hydrogen spillover mechanism and its contribution to HER activity, a series of targeted experiments was performed. The presence of spillover H* was visually tracked using

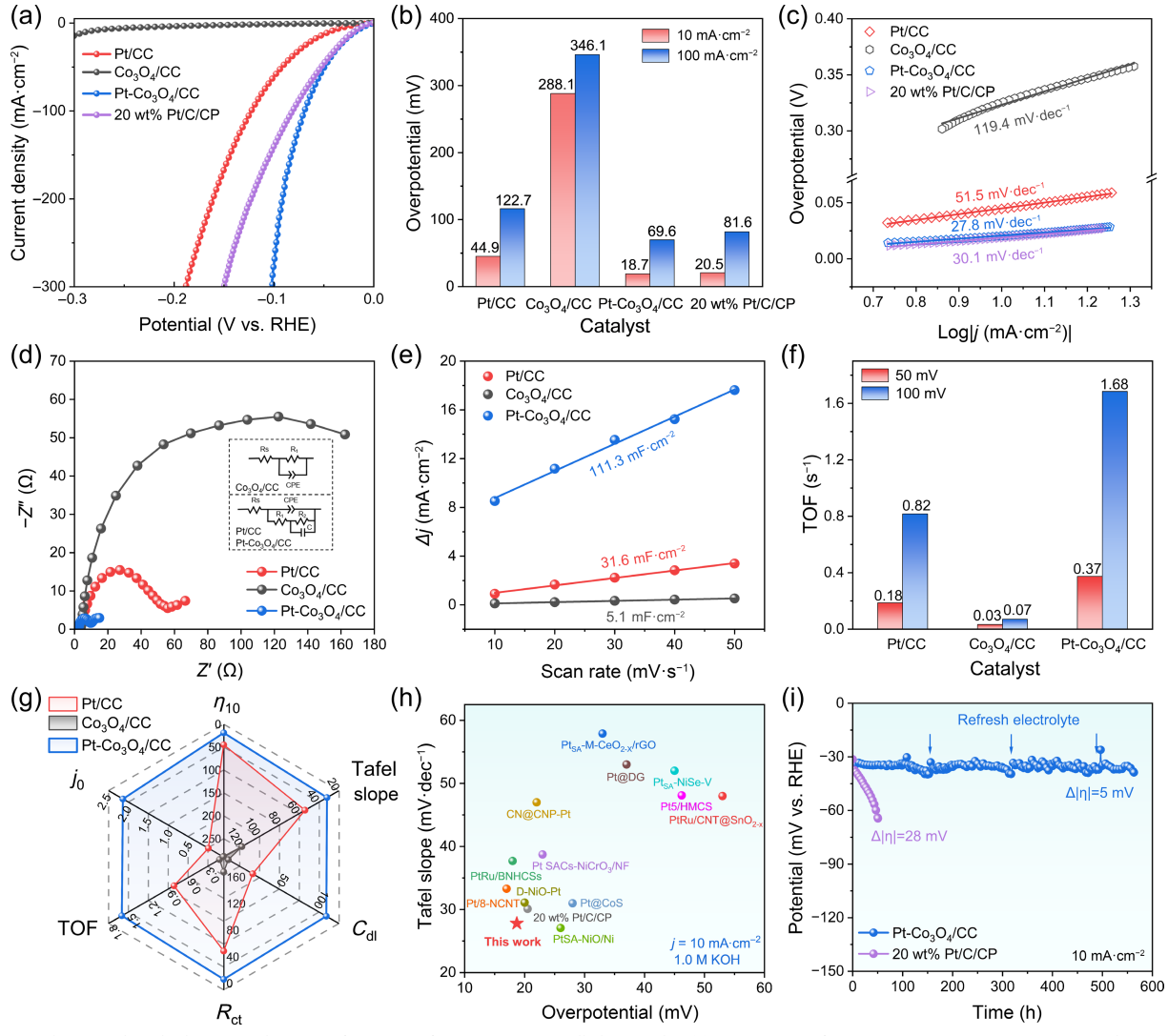

Figure 3 Electrocatalytic hydrogen evolution performance of Pt-Co_3O_4/CC in alkaline media. (a) LSV curves of Pt/CC, Co_3O_4/CC, Pt-Co_3O_4/CC, and commercial 20% Pt/C/CP in 1.0 M KOH electrolyte at a scan rate of 5 mV·s^{-1}. (b) Comparison of the overpotentials of different electrocatalysts at current densities of 10 and 100 mA·cm^{-2}. (c) The Tafel plots of Pt/CC, Co_3O_4/CC, Pt-Co_3O_4/CC, and commercial 20% Pt/C/CP in 1.0 M KOH electrolyte. (d) Nyquist plots of Pt/CC, Co_3O_4/CC, and Pt-Co_3O_4/CC in 1.0 M KOH at –0.02 V vs. RHE. The inset shows the corresponding equivalent circuit. (e) Plots of the current density difference of anodic and cathodic at 0.08 V vs. RHE against the scan rate for Pt/CC, Co_3O_4/CC, and Pt-Co_3O_4/CC to estimate their C_{dl} values. (f) TOF values of Pt/CC, Co_3O_4/CC, and Pt-Co_3O_4/CC at overpotentials of 50 and 100 mV. (g) Comparison of the electrocatalytic performance of Pt/CC, Co_3O_4/CC, and Pt-Co_3O_4/CC. (h) The comparison of the Tafel slope and overpotential of Pt-Co_3O_4/CC and reported Pt-based catalysts. (i) Chronopotentiometry curves of corresponding catalysts at –10 mA·cm^{-2} in 1.0 M KOH electrolyte.

a WO_3 indicator. Spillover H* reacts with WO_3, forming H_xWO_3 and causing a distinct color change from pale yellow to deep blue [46]. As shown in Fig. 4(a), after HER testing, the WO_3-Pt-Co_3O_4/CC mixture (synthesis details and related discussion are provided in the experimental section and Fig. S22 in the ESM) exhibited a pronounced deep blue color, indicating the possible involvement of hydrogen spillover. In contrast, the WO_3-Pt/CC and WO_3-Co_3O_4/CC mixtures exhibit no color changes under identical conditions, indicating negligible spillover H* generation [47]. Furthermore, the dark blue coloration observed in the mixture of Pt-Co_3O_4 and WO_3 after H_2 treatment indicates the occurrence of hydrogen spillover (Fig. S23 in the ESM). The presence of hydrogen spillover was further corroborated by determining the reaction order derived from LSV measurements in KOH electrolytes with varying pH values (Fig. S24 in the ESM). As illustrated in Fig. 4(b), the reaction orders for Pt/CC, Co_3O_4/CC, and Pt-Co_3O_4/CC are calculated to be 0.66, 0.53, and 1.63, respectively. Notably, the reaction order for Pt-Co_3O_4/CC approaches close to the theoretical value of 2, which is characteristic of HER mechanisms involving hydrogen spillover, and aligns well with previously reported values for spillover-based systems [48, 49]. To identify the active sites responsible for the enhanced HER performance of the Pt-Co_3O_4/CC catalyst, selective poisoning experiments were carried out using ethylenediaminetetraacetic acid (EDTA) as a chemical probe [50]. The results demonstrate that EDTA significantly suppressed the HER activity of Co_3O_4/CC while exerting minimal effect on Pt/CC, confirming its selective poisoning of active sites on Co_3O_4 (Fig. S25 in the ESM). Upon addition of EDTA during HER measurements of Pt-Co_3O_4/CC, a cathodic overpotential shift of 46.4 mV in η_{10} is observed, suggesting that Co_3O_4, in addition to Pt, plays a key role in enhanced HER performance (Fig. 4(c)). These findings suggest that Co_3O_4 may serve as a key reaction site in the hydrogen spillover process.

In situ Fourier transform infrared spectroscopy (FTIR) was employed to further elucidate the mechanisms underlying

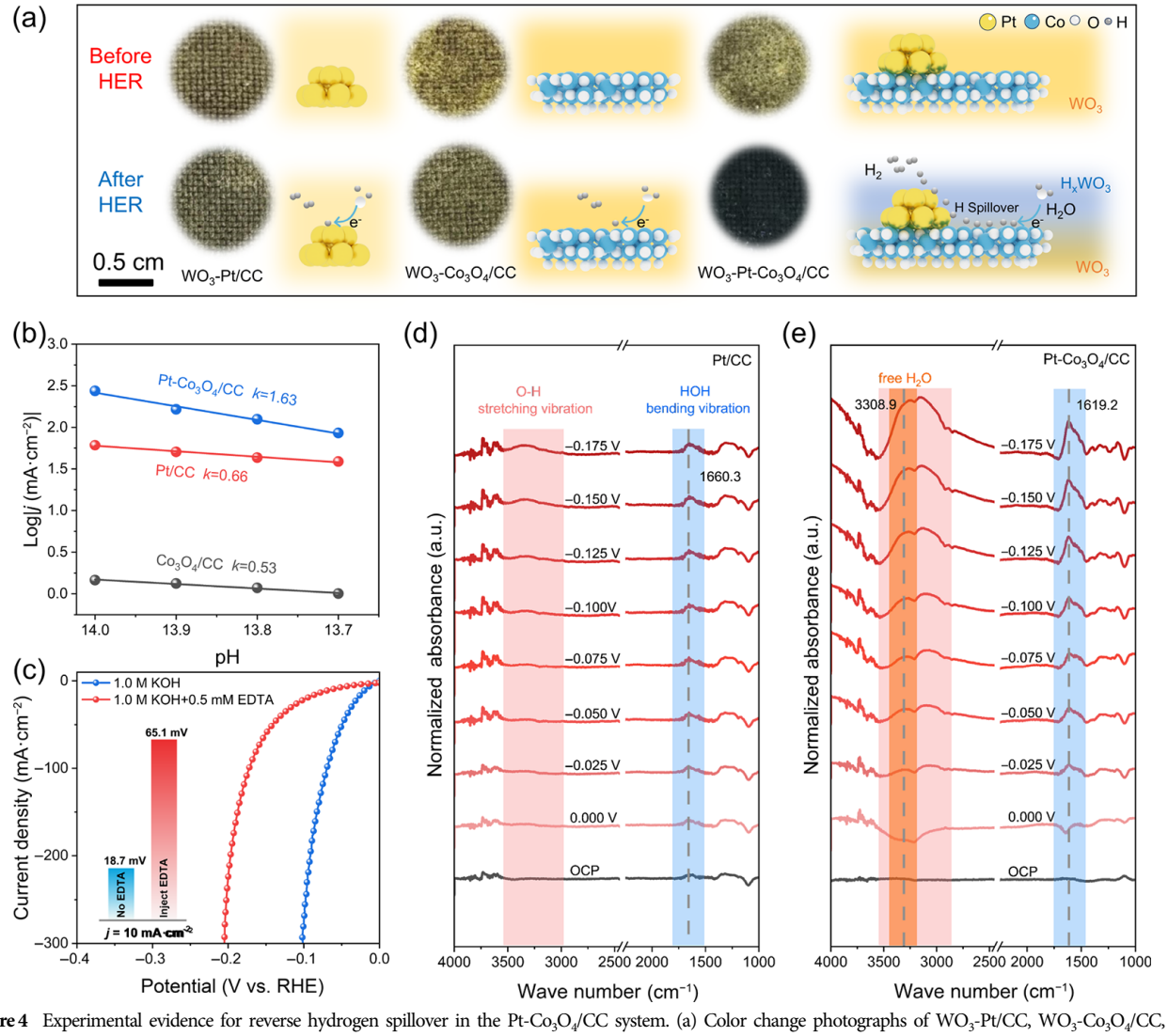

Figure 4 Experimental evidence for reverse hydrogen spillover in the Pt-Co_3O_4/CC system. (a) Color change photographs of WO_3-Pt/CC, WO_3-Co_3O_4/CC, and WO_3/Pt-Co_3O_4/CC catalysts before and after the HER. (b) Plots of Log |*j*@-100 mV vs. RHE| versus pH for Pt/CC, Co_3O_4/CC, and Pt-Co_3O_4/CC. (c) Catalyst poisoning experiment for Pt-Co_3O_4/CC in 1.0 M KOH with the addition of 10 mM of EDTA. *In situ* FTIR spectra of (d) Pt/CC and (e) Pt-Co_3O_4/CC from 0 to −0.175 V vs. RHE in 1.0 M KOH solution.

hydrogen spillover. As shown in Fig. 4(d), *in situ* FTIR spectra of the Pt/CC catalyst recorded in 1.0 M KOH over a potential range of 0 to −0.175 V vs. RHE exhibit two distinct vibrational features associated with adsorbed water molecules on the catalyst surface. The absorption band at approximately 1660.3 cm^{-1} is assigned to the HOH bending mode, whereas the broad band spanning 2800–3600 cm^{-1} originates from O-H stretching vibrations [51]. Compared to Pt/CC, the Pt-Co_3O_4/CC catalyst displays significantly enhanced vibrational signals corresponding to interfacial water species and a pronounced red shift in the characteristic bands (Fig. 4(e)). This indicates that the introduction of Co_3O_4 not only promotes water adsorption but also weakens the O-H bond strength, thereby facilitating water activation and dissociation [52]. Furthermore, the O-H stretching vibration band in the spectrum of Pt-Co_3O_4/CC exhibits clear splitting, implying the coexistence of multiple configurations of water molecules at the interface. The peak observed at 3308.9 cm^{-1}, attributed to non-hydrogen-bonded (free) water, serves as a key reactant in the Volmer step [53]. The substantial increase in its content accelerates the Volmer step. These results suggest that the incorporation of Co_3O_4 induces a restructuring of interfacial water, thus optimizing the local microenvironment for the Volmer process and enhancing its kinetics.

In summary, based on the validation of the hydrogen spillover effect, EDTA molecular probe experiments, and *in situ* FTIR analysis, it can be concluded that the initial adsorption and dissociation of H_2O, i.e., the Volmer step, predominantly occur on the Co_3O_4 surface. The generated H* intermediates subsequently migrate to Pt sites through a reverse hydrogen spillover process, where hydrogen desorption takes place. Collectively, these results demonstrate that the overall reaction proceeds through a reverse hydrogen spillover mechanism.

The hydrogen spillover effect is further elucidated through *in situ* hydrogen adsorption and desorption behavior of the catalyst. *In situ* electrochemical impedance spectroscopy (EIS) measurements were performed to investigate hydrogen adsorption kinetics. The Bode plots (Figs. 5(a)–5(c)) reveal that Pt-Co_3O_4/CC exhibits a lower phase angle, indicating more charge participation in the Faradaic process (HER) rather than being stored at the electrode-electrolyte interface to form C_{dl} [54]. Furthermore, the rapid phase angle variation at high-frequency region with applied potential suggests dynamic interfacial behavior, further supporting

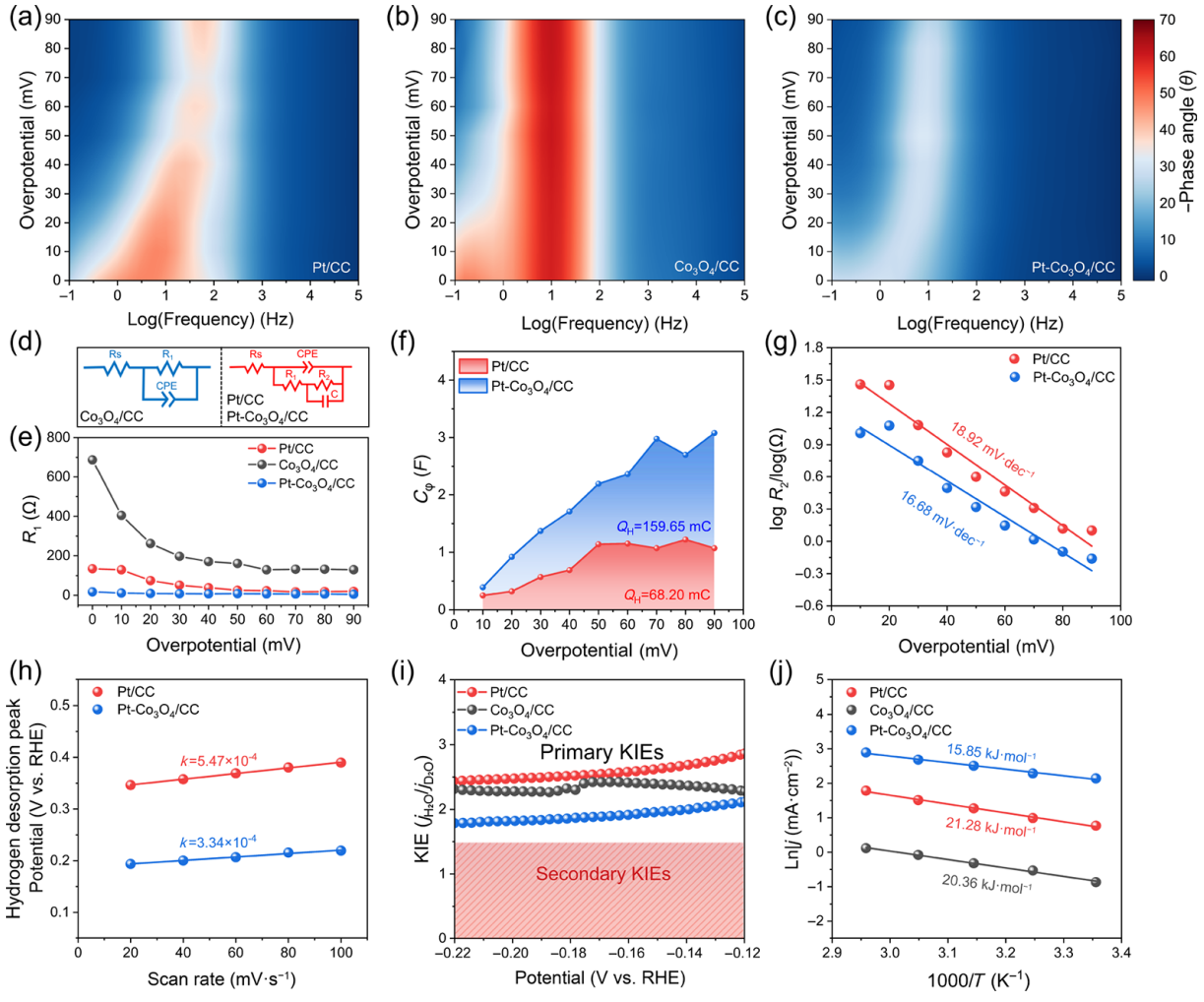

Figure 5 Hydrogen adsorption/desorption behavior and kinetic analysis of the Pt-Co_3O_4 heterostructure. Bode plots of (a) Pt/CC, (b) Co_3O_4/CC, and (c) Pt-Co_3O_4/CC in 1.0 M KOH electrolyte at various potentials. (d) The equivalent circuit was used for modeling the measured electrochemical response. (e) The resistance of the electrode interface reaction on Pt/CC, Co_3O_4/CC, and Pt-Co_3O_4/CC. (f) Plots of C_φ vs. overpotential of Pt/CC and Pt-Co_3O_4/CC during HER in 1.0 M KOH electrolyte. (g) EIS-derived Tafel plots of Pt/CC and Pt-Co_3O_4/CC obtained from the hydrogen adsorption resistance R_2. (h) Plots of hydrogen desorption peak position vs. scan rates of Pt/CC and Pt-Co_3O_4/CC. (i) Calculated KIE values of Pt/CC, Co_3O_4/CC, and Pt-Co_3O_4/CC, respectively. (j) Typical Arrhenius plots for Pt/CC, Co_3O_4/CC, and Pt-Co_3O_4/CC.

hydrogen migration on the Pt-Co_3O_4/CC surface (Fig. S26(a) in the ESM) [48]. To further quantify the charge and ion transfer dynamics during the reaction, the EIS data were fitted using equivalent circuit models, with circuit selection carefully adapted to the distinct features of the Nyquist plots for each catalyst (Figs. S26(b)–S26(d) in the ESM). The Nyquist plot of Co_3O_4/CC exhibits a single semicircular arc, which was modeled using a classical Randles circuit. In contrast, the Nyquist plots of Pt/CC and Pt-Co_3O_4/CC display two distinct semicircular arcs, requiring the application of a double parallel equivalent circuit for accurate fitting (Fig. 5(d)). In the double parallel equivalent circuit, R_S denotes the solution resistance. The first parallel components are associated with the charge transfer at the electrode-electrolyte interface. Specifically, CPE and R_1 represent the double-layer capacitance and the charge transfer resistance during the Faradaic reaction, respectively. The second parallel components are related to the adsorption behavior of reaction intermediates at the electrode-electrolyte interface, with R_2 representing the hydrogen adsorption resistance and C_φ accounting for the pseudo-capacitance from the adsorption/desorption processes of intermediates [55]. Fitting parameters are summarized in Tables S3 and S4 in the ESM.

Pt-Co_3O_4/CC exhibits the lowest R_1 values across all tested overpotentials, indicating superior HER charge-transfer kinetics (Fig. 5(e)). Furthermore, with increasing overpotential, R_2 gradually decreases, and the second semicircle in the low-frequency region diminishes, indicating saturation of hydrogen adsorption on the catalyst surface at higher overpotentials. To quantify this process, the hydrogen adsorption charge (Q_H) is determined by integrating the C_φ versus overpotential curve, which corresponds to the amount of adsorbed hydrogen during the HER. The Q_H values for Pt/CC and Pt-Co_3O_4/CC are found to be 68.20 and 159.65 mC, respectively, demonstrating that Pt-Co_3O_4/CC has superior hydrogen adsorption capacity (Fig. 5(f)). The Tafel slopes derived from EIS, obtained by plotting log R_2 against overpotential, offer insight into the hydrogen adsorption kinetics of Pt-Co_3O_4/CC and Pt/CC [25]. Notably, the Tafel slope of Pt-Co_3O_4/CC (16.68 mV·dec^{-1}) is considerably lower than that of Pt/CC (18.92 mV·dec^{-1}), indicating more favorable hydrogen adsorption kinetics (Fig. 5(g)).

To investigate hydrogen desorption behavior, *operando* cyclic voltammetry (CV) measurements were conducted on Pt/CC, Co_3O_4/CC, and Pt-Co_3O_4/CC. As shown in Fig. S27 in the ESM, a weak hydrogen desorption peak was observed on Pt/CC, while no

discernible signal was detected on Co_3O_4/CC. These results suggest that both electrocatalysts exhibit relatively low hydrogen desorption activity, with Pt sites demonstrating superior hydrogen desorption capability compared to Co sites. Notably, Pt-Co_3O_4/CC exhibits a distinct hydrogen desorption peak around 0.2 V vs. RHE, likely due to the hydrogen spillover effect facilitating the desorption of hydrogen. The kinetics of hydrogen desorption are evaluated by linearly fitting the peak position as a function of scan rate. With increasing scan rate, the current response lags behind the applied potential, leading to a shift in the desorption peak to higher potentials. Therefore, a smaller shift in the peak potential, reflected by a lower slope of the fitted line, indicates faster hydrogen desorption kinetics. As shown in Fig. 5(h), the slope for Pt-Co_3O_4/CC (3.34×10^{-4}) is significantly lower than that for Pt/CC (5.47×10^{-4}), suggesting significantly enhanced hydrogen desorption kinetics on Pt-Co_3O_4/CC [56].

Deuterium kinetic isotope effects (KIEs) experiments provide valuable insights into the hydrogen/proton transfer dynamics involved in the HER. Due to the greater mass of deuterium, hydrogen/proton migration proceeds more slowly in deuterated water (D_2O) than in protonated water (H_2O), thereby enabling D_2O to effectively retard the kinetics of hydrogen/proton transfer. Importantly, KIEs experiments reveal the rate-determining step (RDS) in the catalytic process. A primary KIE value exceeding 1.5 indicates that hydrogen/proton transfer is either part of the RDS or exerts a substantial influence on it during HER [57]. As shown in Fig. S28 in the ESM, the LSV curves of Pt/CC, Co_3O_4/CC, and Pt-Co_3O_4/CC in 1.0 M NaOH/H_2O exhibit higher HER activity compared to those obtained in 1.0 M NaOD/D_2O. The primary KIEs values for Pt/CC, Co_3O_4/CC, and Pt-Co_3O_4/CC are 2.4–2.8, 2.2–2.4, and 1.7–2.1, respectively, all exceeding 1.5, suggesting that hydrogen/proton transfer may be the RDS (Fig. 5(i)). Moreover, the Pt-Co_3O_4/CC catalyst exhibits the lowest KIE value compared to Pt/CC and Co_3O_4/CC, indicating the most rapid hydrogen/proton transfer kinetics. Polarization curves measured at different temperatures were analyzed to extract the apparent activation energy (E_a) using the Arrhenius equation, providing insight into the kinetic barriers of the HER process (Fig. S29 in the ESM). The Pt-Co_3O_4/CC exhibits a markedly lower E_a of 15.85 kJ·mol^{-1} compared with Pt/CC (21.28 kJ·mol^{-1}) and Co_3O_4/CC (20.36 kJ·mol^{-1}), indicating significantly accelerated HER kinetics on the heterointerface (Fig. 5(j)). In summary, the unique hydrogen adsorption and desorption behavior observed on Pt-Co_3O_4/CC provides further experimental evidence for interfacial hydrogen spillover. Meanwhile, comprehensive kinetic analyses collectively indicate that the HER kinetics on this heterostructure catalyst are markedly enhanced.

2.5 DFT calculations

Density functional theory (DFT) calculations were conducted to systematically explore the origin of the superior HER activity observed in Pt-Co_3O_4/CC, as well as to identify potential hydrogen spillover pathways (Fig. S30 in the ESM). Charge density difference analysis reveals pronounced interfacial charge redistribution in the Pt-Co_3O_4 heterostructure, where electron transfer from Co_3O_4 to Pt leads to the formation of an electron-rich Pt region and an electron-depleted Co_3O_4 region, thereby establishing a BEF across the interface (Fig. 6(a)). This phenomenon is fully consistent with the XPS, UPS, and work function results. Projected density of states (PDOS) analysis provides orbital-level insights into the functional specialization of the Pt-Co_3O_4 heterostructure. As shown in Figs. 6(b) and 6(c), the Co d-band center (–1.47 eV) lies closer to the Fermi level than that of Pt (–2.24 eV), endowing Co_3O_4 with stronger orbital interactions with H_2O molecules, thereby favoring water adsorption and activation. In contrast, the more negative d-band center of Pt leads to moderated H* binding, which facilitates hydrogen recombination and desorption [48]. To corroborate these electronic insights, we computed the H_2O adsorption energies and dissociation barriers at the Co_3O_4 and Pt sites within the Pt-Co_3O_4 heterostructure. The Co_3O_4 site exhibits a much more negative H_2O adsorption energy (–1.23 eV vs. –0.31 eV for Pt) and a lower O-H dissociation barrier (0.55 eV vs. 0.86 eV), confirming its superior water activation ability (Fig. S31 in the ESM, Figs. 6(d) and 6(e)). Notably, introducing oxygen vacancies into the Co_3O_4 lattice further enhances H_2O adsorption under alkaline conditions (Fig. S32 in the ESM). Moreover, the near-zero ΔG_{H^*} on Pt (0.01 eV) identifies it as the ideal site for H_2 generation and release (Fig. 6(f)). Accordingly, H* generated from water dissociation on Co_3O_4 are required to migrate to Pt sites for hydrogen recombination and subsequent desorption.

It is worth emphasizing that the realization of such effective interfacial synergy is not spontaneous but critically relies on the efficient migration of interfacial H*. When this migration is sluggish, H* accumulation and site poisoning on Co_3O_4 will take place, or the Pt sites will experience a shortage of H* supply. Therefore, understanding the kinetics of H* migration is essential for evaluating the efficiency of interfacial synergy. Thus, we computed the H* migration pathway in the Pt-Co_3O_4 heterostructure. The migration from site 1 to site 2 corresponds to H* migration on the Co_3O_4 surface, while site 2 to site 3 represents cross-interface H* migration, followed by H* migration on the Pt surface (site 3 to site 4) (Fig. 6(g)). On the Co_3O_4 surface, H* migration between adjacent sites requires overcoming an energy barrier of 0.27 eV (Fig. 6(h)). Notably, the cross-interface migration barrier is substantially reduced to 0.13 eV, indicating that the heterointerface serves as a fast channel for H* migration. This pronounced kinetic enhancement originates from the BEF directed from Co_3O_4 to Pt. The H* species, produced from water dissociation on Co_3O_4, is thus electrostatically "pushed" by the positively charged Co_3O_4 region and "pulled" by the negatively charged Pt domain. This field-driven force stabilizes the transition state for the interfacial crossing, effectively reducing the kinetic barrier. As a result, the maximum energy barrier along the reverse hydrogen spillover pathway (0.27 eV) is lower than that for direct H desorption from Co_3O_4 (0.37 eV), providing compelling kinetic evidence for a BEF-driven reverse hydrogen spillover mechanism.

It should be emphasized that the BEF strength plays a pivotal role in governing the kinetics of BEF-driven reverse hydrogen spillover. This is reflected in the pronounced non-monotonic dependence of HER activity on BEF strength, with optimal activity achieved at an intermediate BEF, rather than following a simple "stronger-is-better" trend. Mechanistically, a weak BEF is insufficient to drive hydrogen migration from Co_3O_4 to Pt, resulting in hydrogen accumulation on the Co_3O_4 surface. In contrast, an excessively strong BEF may lead to excessive accumulation of hydrogen on Pt, thereby disrupting the kinetic coupling between intermediate transfer and subsequent reaction steps. Therefore, an appropriately tuned BEF is essential for directing interfacial hydrogen migration, establishing an efficient intermediate transport pathway, and maintaining the kinetic matching between water dissociation and hydrogen desorption.

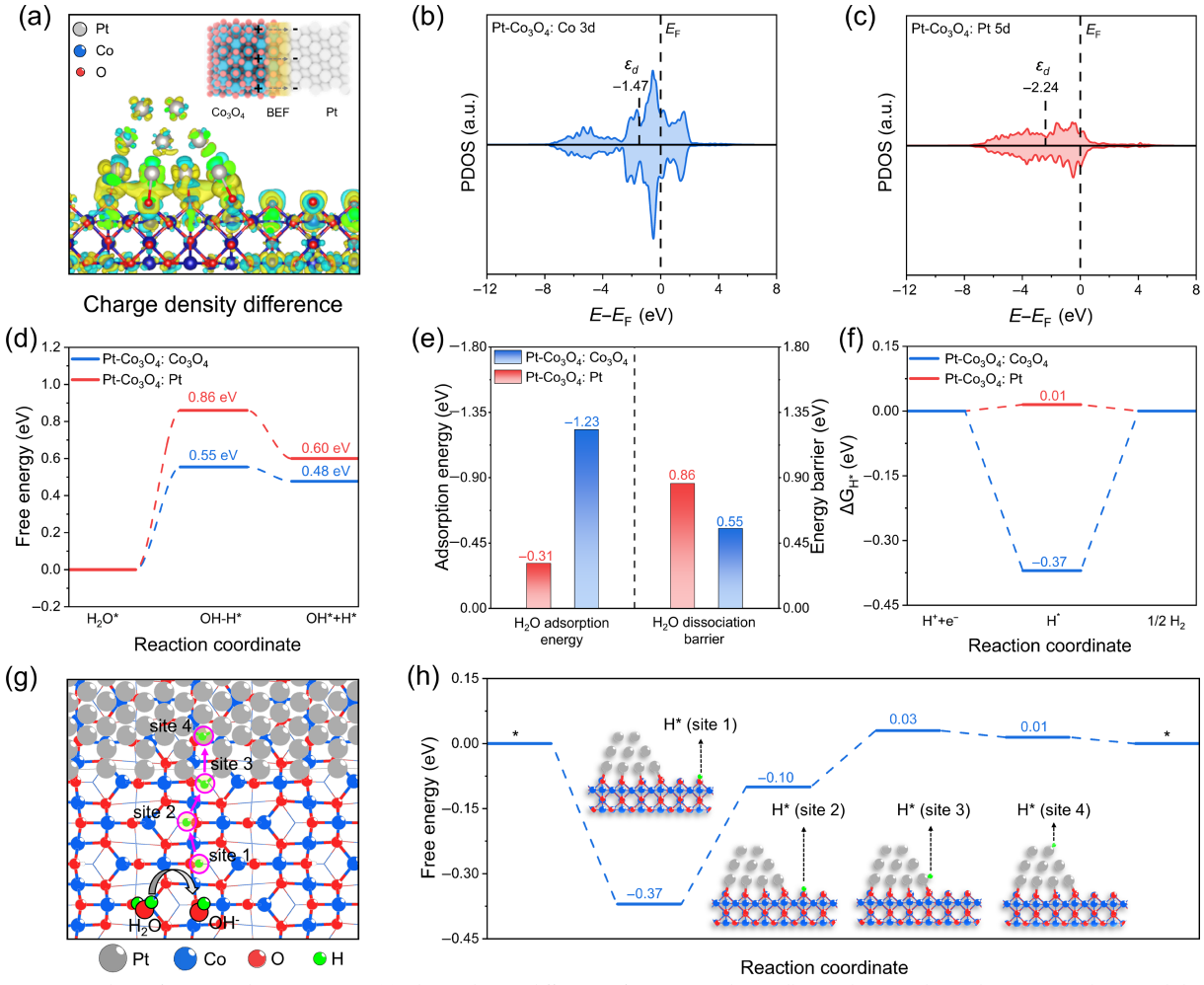

Figure 6 DFT analysis of Pt-Co_3O_4 heterostructure. (a) Charge density difference of Pt-Co_3O_4, where yellow and cyan indicate charge accumulation and depletion, respectively. Projected density of states (PDOS) calculated for (b) Co and (c) Pt atoms in Pt-Co_3O_4. The dashed lines denote the Co 3d and Pt 5d band centers. (d) Reaction energy diagram for water dissociation on Pt and Co_3O_4 of Pt-Co_3O_4. (e) Calculated H_2O adsorption energy and energy barrier of H_2O dissociation on Pt and Co_3O_4 of Pt-Co_3O_4. (f) Calculated Gibbs free energy diagrams for HER on Pt and Co_3O_4 of Pt-Co_3O_4. (g) Schematic illustration and (h) hydrogen migration energies on the Pt-Co_3O_4 surface.

2.6 AEM electrolyzer performance

Motivated by its exceptional alkaline HER performance, the application of Pt-Co_3O_4/CC for alkaline seawater electrolysis was investigated. This system offers two critical advantages: strongly alkaline conditions precipitate Mg^{2+} and Ca^{2+} ions before electrolysis, preventing active-site blockage (Fig. S33 in the ESM), while effectively suppressing detrimental chlorine evolution. These advantages establish alkaline seawater electrolysis as a promising route for industrial hydrogen production, combining operational stability with environmental safety at high current densities. To evaluate the HER performance of the Pt-Co_3O_4/CC electrode in chloride ion solutions and natural seawater with complex ionic compositions, simulated alkaline seawater (1.0 M KOH + 0.5 M NaCl) and natural alkaline seawater (1.0 M KOH + seawater, collected from the Bohai Sea) were used as electrolytes. Figure 7(a) shows the polarization curves of the Pt-Co_3O_4/CC electrode in alkaline electrolyte, simulated alkaline seawater, and natural alkaline seawater. Compared with pure alkaline electrolyte, a decrease in HER activity is observed in both simulated and natural alkaline seawater. Specifically, in simulated alkaline seawater, the Pt-Co_3O_4/CC electrode delivered current densities of 10, 100, and 500 mA·cm^{-2} at overpotentials of 18.8, 71.7, and 119.7 mV, respectively (Fig. 7(b)). The overpotentials required to reach 10 and 100 mA·cm^{-2} are comparable to those in pure alkaline solution, while the slight increase observed at 500 mA·cm^{-2} is mainly attributed to the competitive adsorption of chloride ions, which occupy part of the active sites and increase the R_{ct} [58]. The gradual decrease in HER activity with increasing chloride ion concentration in the electrolyte further supports this interpretation (Fig. S34 in the ESM). In natural alkaline seawater, the electrode achieves the same current densities at overpotentials of 27.3, 75.0, and 130.6 mV, respectively, with the further decrease in HER activity likely caused by residual hard cations that block the active sites (Fig. S35 in the ESM). Nonetheless, the electrode maintains excellent performance, demonstrating its strong catalytic stability under harsh conditions. To assess the practical potential of the Pt-Co_3O_4/CC electrode, we constructed an anion exchange membrane water electrolyzer (AEMWE) for alkaline natural seawater electrolysis (Fig. 7(c), Fig. S36 in the ESM), using Pt-Co_3O_4/CC as the cathode and NiFe LDH/NF as the anode (Pt-Co_3O_4||NiFe LDH AEMWE). Figure 7(d) shows the polarization curves of the electrolyzer at various temperatures. At a current density of 1 A·cm^{-2}, the cell voltages were 1.82, 1.79, and 1.76 V at 60, 70, and 80 °C, respectively, approaching the U.S. Department of Energy's 2026 target and underscoring its promise for practical applications [59]. For comparison, an AEMWE was assembled

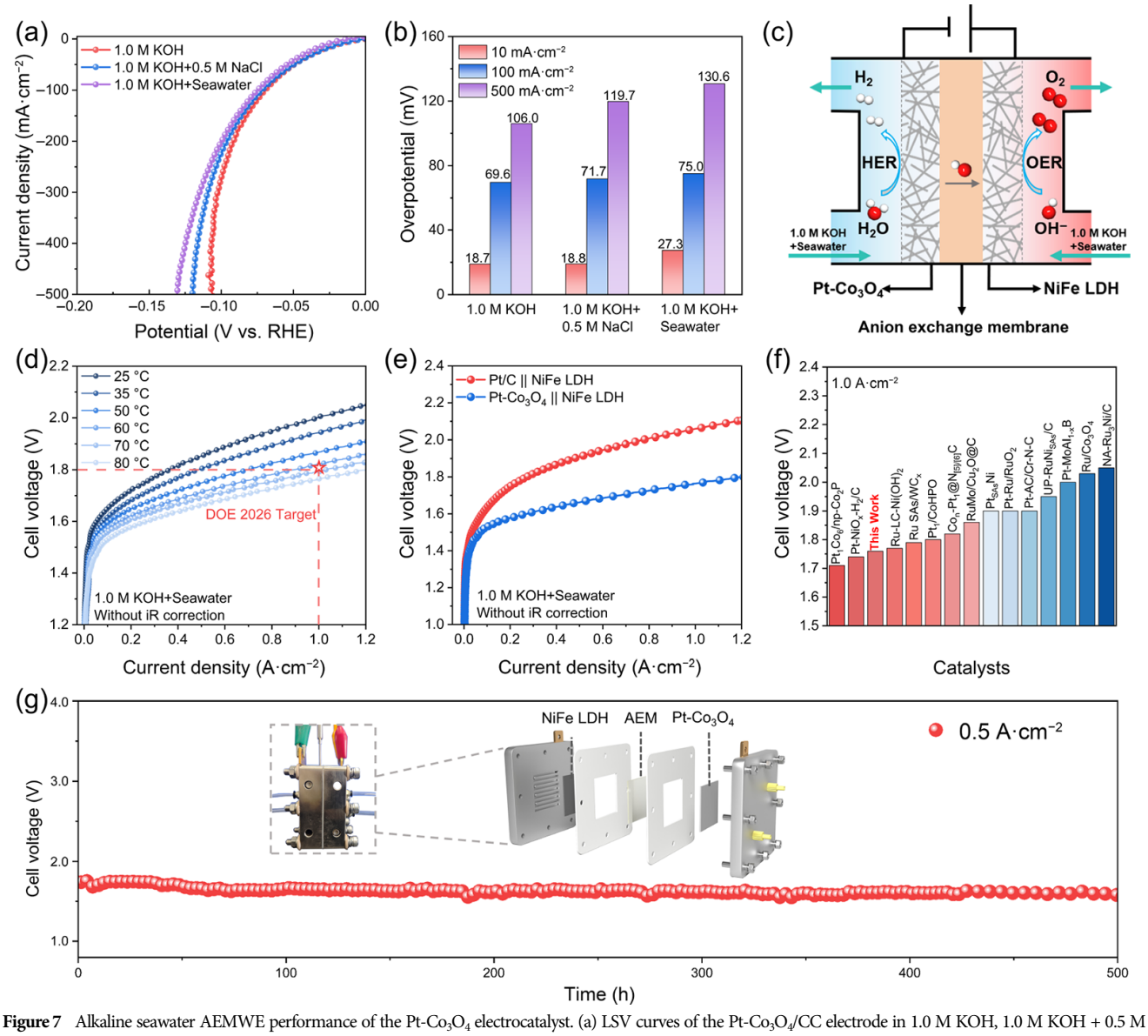

Figure 7 Alkaline seawater AEMWE performance of the Pt-Co_3O_4 electrocatalyst. (a) LSV curves of the Pt-Co_3O_4/CC electrode in 1.0 M KOH, 1.0 M KOH + 0.5 M NaCl, and 1.0 M KOH + seawater electrolytes. (b) Comparison of the overpotentials of the Pt-Co_3O_4/CC electrode at current densities of 10, 100, and 500 mA·cm^{-2} in different electrolytes. (c) Schematic illustration of an AEMWE with a Pt-Co_3O_4 cathode and a NiFe LDH anode. (d) Polarization curves of the Pt-Co_3O_4||NiFe LDH AEMWE operated in 1.0 M KOH + seawater electrolyte at different temperatures. (e) Comparison of the performance of Pt-Co_3O_4||NiFe LDH and Pt/C||NiFe LDH AEMWEs operated in 1.0 M KOH + seawater at 80 °C. (f) Comparison of cell voltage at a current density of 1 A·cm^{-2} for our electrolyzer versus state-of-the-art water and seawater electrolyzers. (g) Durability test of the Pt-Co_3O_4||NiFe LDH AEMWE in 1.0 M KOH + seawater at 60 °C.

using a commercial Pt/C electrode as the cathode and NiFe LDH/NF as the anode (Pt/C||NiFe LDH AEMWE), and its overall water-splitting performance was evaluated at various temperatures (Fig. S37(a) in the ESM). At a current density of 1 A·cm^{-2} and 80 °C, the Pt/C||NiFe LDH AEMWE required a cell voltage of 2.05 V, 0.29 V higher than that the Pt-Co_3O_4||NiFe LDH AEMWE, demonstrating the superior performance of the Pt-Co_3O_4||NiFe LDH AEMWE (Fig. 7(e)). Compared with other reported state-of-the-art AEMWE catalysts, our catalyst also exhibits superior performance (Fig. 7(f), Table S5 in the ESM). Furthermore, under a constant current density of 500 mA·cm^{-2} at 60 °C, the Pt-Co_3O_4||NiFe LDH AEMWE demonstrated excellent stability, maintaining steady operation for 500 hours (Fig. 7(g)). By comparison, the Pt/C||NiFe LDH AEMWE exhibited significant performance degradation after only 1.5 hours (Fig. S37(b) in the ESM).

3 Conclusion

In this work, we demonstrate that engineering a high-speed reverse hydrogen spillover channel is the key to specifically addressing a persistent yet overlooked kinetic bottleneck in conventional dual-site alkaline HER catalysts. We design and construct an atomically coupled Pt-Co_3O_4/CC heterostructure featuring dual active sites. In this design, Co_3O_4 preferentially adsorbs and dissociates water to generate H* intermediates, while Pt provides hydrogen adsorption sites with a near-zero ΔG_{H^*} for efficient H_2 recombination and desorption. More importantly, the BEF, induced by the work function difference at the interface, drives the directional migration of H* from Co_3O_4 to Pt and lowers the migration energy barrier to 0.13 eV. By tuning the oxygen vacancy concentration in Co_3O_4 to modulate the BEF strength, we further reveal that HER activity exhibits a non-monotonic dependence on the BEF, where a moderate BEF

facilitates balanced H* migration and transforms the heterointerface into an efficient H* migration channel, which in turn accelerates the overall reaction kinetics. As a result, Pt-Co_3O_4/CC achieves 10 mA·cm^{-2} at 18.7 mV with a Tafel slope of 27.8 mV·dec^{-1} in 1.0 M KOH. When integrated into an AEM electrolyzer for natural alkaline seawater splitting, it delivers 1 A·cm^{-2} at 1.76 V and operates stably for over 500 hours, demonstrating strong potential for industrial application. This work establishes interfacial H* transport kinetics as an independent and tunable design parameter, with reverse hydrogen spillover playing a central role, thereby offering a general strategy for advancing multi-step electrocatalytic reactions involving coupled adsorption, transformation, and desorption processes.

Acknowledgements

This work was supported by the National Natural Science Foundation of China (No. U24A2023).

Declaration of conflicting interests

The authors declare no conflicting interests regarding the content of this article.

Data availability

All data needed to support the conclusions in the paper are presented in the manuscript and/or the Supplementary Materials. Additional data related to this paper may be requested from the corresponding author upon request.

Electronic Supplementary Material Supplementary material (detailed experimental procedures and DFT calculations. Raman spectroscopy, SEM, TEM, XPS and electrochemical analysis of electrocatalysts) is available in the online version of this article at https://doi.org/10.26599/NRE.2026.9120233.

References

[1] Turner, J. A. Sustainable hydrogen production. *Science* **2004**, *305*, 972–974.

[2] Roger, I.; Shipman, M. A.; Symes, M. D. Earth-abundant catalysts for electrochemical and photoelectrochemical water splitting. *Nat. Rev. Chem.* **2017**, *1*, 0003.

[3] Yu, L.; Zhu, Q.; Song, S. W.; McElhenny, B.; Wang, D. Z.; Wu, C. Z.; Qin, Z. J.; Bao, J. M.; Yu, Y.; Chen, S. et al. Non-noble metal-nitride based electrocatalysts for high-performance alkaline seawater electrolysis. *Nat. Commun.* **2019**, *10*, 5106.

[4] Anantharaj, S.; Noda, S.; Jothi, V. R.; Yi, S.; Driess, M.; Menezes, P. W. Strategies and perspectives to catch the missing pieces in energy-efficient hydrogen evolution reaction in alkaline media. *Angew. Chem., Int. Ed.* **2021**, *60*, 18981–19006.

[5] Zhou, C. H.; Shi, J.; Dong, Z. Q.; Zeng, L. Y.; Chen, Y.; Han, Y.; Li, L.; Zhang, W. Y.; Zhang, Q. H.; Gu, L. et al. Oxophilic gallium single atoms bridged ruthenium clusters for practical anion-exchange membrane electrolyzer. *Nat. Commun.* **2024**, *15*, 6741.

[6] Sun, X. R.; Ge, B. X.; Xue, S. K.; Zhang, J. C.; Chen, J. Y.; Cheng, W. R.; Wang, S. B.; Yu, Z. Y.; Lu, X. F. Lattice-matched Cu_3Pd@α-MoC_{1-x} heterointerfaces boost alkaline hydrogen evolution by accelerating water dissociation and optimizing hydrogen adsorption energy. *App. Catal. B: Environ. Energy* **2026**, *386*, 126418.

[7] Yu, L.; Wu, L. B.; McElhenny, B.; Song, S. W.; Luo, D.; Zhang, F. H.; Yu, Y.; Chen, S.; Ren, Z. F. Ultrafast room-temperature synthesis of porous S-doped Ni/Fe (Oxy)hydroxide electrodes for oxygen evolution catalysis in seawater splitting. *Energy Environ. Sci.* **2020**, *13*, 3439–3446.

[8] Zang, W. J.; Sun, T.; Yang, T.; Xi, S. B.; Waqar, M.; Kou, Z. K.; Lyu, Z.; Feng, Y. P.; Wang, J.; Pennycook, S. J. Efficient hydrogen evolution of oxidized Ni–N_3 defective sites for alkaline freshwater and seawater electrolysis. *Adv. Mater.* **2021**, *33*, 2003846.

[9] Chen, J. D.; Chen, C. H.; Qin, M. K.; Li, B.; Lin, B. B.; Mao, Q.; Yang, H. B.; Liu, B.; Wang, Y. Reversible hydrogen spillover in Ru–WO_{3-x} enhances hydrogen evolution activity in neutral pH water splitting. *Nat. Commun.* **2022**, *13*, 5382.

[10] Ren, H.; Zhang, Z. H.; Geng, Z. X.; Wang, Z.; Shen, F. Y.; Liang, X. H.; Cai, Z. J.; Wang, Y. F.; Cheng, D.; Cao, Y. N. et al. Gradient OH desorption facilitating alkaline hydrogen evolution over ultrafine quinary nanoalloy. *Adv. Energy Mater.* **2024**, *14*, 2400777.

[11] Hou, L. Q.; Li, C.; Jang, H.; Kim, M. G.; Jiang, J. Z.; Cho, J.; Liu, S. G.; Liu, X. E. Rationally designed Mo/Ru-based multi-site heterogeneous electrocatalyst for accelerated alkaline hydrogen evolution reaction. *Adv. Mater.* **2024**, *36*, 2410039.

[12] Du, Y. B.; Wang, H. N.; Chen, J. Y.; Chen, H. X.; Wang, S. B.; Lu, X. F. Ultrafine NiIr nanoclusters confined in hollow mesoporous carbon spheres accelerate alkaline hydrogen evolution. *Chem. Commun.* **2025**, *61*, 17854–17857.

[13] Li, M. F.; Duanmu, K. N.; Wan, C. Z.; Cheng, T.; Zhang, L.; Dai, S.; Chen, W. X.; Zhao, Z. P.; Li, P.; Fei, H. L. et al. Single-atom tailoring of platinum nanocatalysts for high-performance multifunctional electrocatalysis. *Nat. Catal.* **2019**, *2*, 495–503.

[14] Hu, Q.; Gao, K. R.; Wang, X. D.; Zheng, H. J.; Cao, J. Y.; Mi, L. R.; Huo, Q. H.; Yang, H. P.; Liu, J. H.; He, C. X. Subnanometric Ru clusters with upshifted d band center improve performance for alkaline hydrogen evolution reaction. *Nat. Commun.* **2022**, *13*, 3958.

[15] Lin, Z. P.; Wang, Z. P.; Gong, J. J.; Jin, T. C.; Shen, S. J.; Zhang, Q. H.; Wang, J. C.; Zhong, W. W. Reversed spillover effect activated by Pt atom dimers boosts alkaline hydrogen evolution reaction. *Adv. Funct. Mater.* **2023**, *33*, 2307510.

[16] Wan, C. Z.; Zhang, Z. S.; Dong, J. C.; Xu, M. J.; Pu, H. T.; Baumann, D.; Lin, Z. Y.; Wang, S. B.; Huang, J.; Shah, A. H. et al. Amorphous nickel hydroxide shell tailors local chemical environment on platinum surface for alkaline hydrogen evolution reaction. *Nat. Mater.* **2023**, *22*, 1022–1029.

[17] Ye, H. Y.; Wu, C. T.; Cao, D. Y.; Zhang, G. R.; Sun, Y. H.; Zhu, Y. C.; Wu, F.; Zhang, Z. H.; Wang, R. M. Atomically resolved two-dimensional amorphous nuclei formed during MoS_2 chemical vapor deposition. *Science* **2026**, *391*, 622–627.

[18] Liu, J. Q.; Sun, X. R.; Lin, K.; Liang, Z.; Xing, W. D.; Chen, J. Y.; Lu, X. F. Optimizing Schottky rectifying effect in PtCu/WO_x heterojunctions to accelerate oxygen reduction kinetics. *Nano Res.* **2026**, *19*, 94908088.

[19] Wang, R. M. The dynamics of the peel. *Nat. Catal.* **2020**, *3*, 333–334.

[20] Karim, W.; Spreafico, C.; Kleibert, A.; Gobrecht, J.; VandeVondele, J.; Ekinci, Y. ; van Bokhoven, J. A. Catalyst support effects on hydrogen spillover. *Nature* **2017**, *541*, 68–71.

[21] Mahdavi-Shakib, A.; Whittaker, T. N.; Yun, T. Y.; Kumar, K. B. S.; Rich, L. C.; Wang, S. G.; Rioux, R. M.; Grabow, L. C.; Chandler, B. D. The role of surface hydroxyls in the entropy-driven adsorption and spillover of H_2 on Au/TiO_2 catalysts. *Nat. Catal.* **2023**, *6*, 710–719.

[22] Liu, T. T.; Gao, W. B.; Wang, Q. Q.; Dou, M. L.; Zhang, Z. P.; Wang, F. Selective loading of atomic platinum on a $RuCeO_x$ support enables stable hydrogen evolution at high current densities. *Angew. Chem., Int. Ed.* **2020**, *59*, 20423–20427.

[23] Huang, J. Z.; Han, J. C.; Wu, T.; Feng, K.; Yao, T.; Wang, X. J.; Liu, S. W.; Zhong, J.; Zhang, Z. H.; Zhang, Y. M. et al. Boosting hydrogen transfer during Volmer reaction at oxides/metal nanocomposites for efficient alkaline hydrogen evolution. *ACS Energy Lett.* **2019**, *4*, 3002–3010.

[24] Shi, W. H.; Liu, H. W.; Zhang, J. W.; Shen, S. Y.; Wang, Y. H.; Guo, Y. Q.; Yue, K. H.; Liang, Z. H.; Zhang, H.; Zhang, L. et al. Roll-to-roll synthesis of multielement heterostructured catalysts. *Nat. Synth.* **2025**, *4*, 836–847.

[25] Li, J. Y.; Hu, J.; Zhang, M. K.; Gou, W. Y.; Zhang, S.; Chen, Z.; Qu, Y. Q.; Ma, Y. Y. A fundamental viewpoint on the hydrogen spillover phenomenon of electrocatalytic hydrogen evolution. *Nat. Commun.* **2021**, *12*, 3502.

[26] Feng, Y.; Li, Z.; Cheng, C. Q.; Kang, W. J.; Mao, J.; Shen, G. R.; Yang, J.; Dong, C. K.; Liu, H.; Du, X. W. Strawberry-like Co_3O_4–Ag bifunctional catalyst for overall water splitting. *Appl. Catal. B: Environ.* **2021**, *299*, 120658.

[27] Zhong, W. Y.; Chen, Y.; Chen, P. Y.; Chen, Q. W.; Yang, C. Z.; Zhang, N.; Liu, X. M.; Lin, Z. Balancing hydrogen evolution and hydrogenation reaction via facet engineering for efficient conversion of nitrate to ammonia in actual wastewater. *Angew. Chem., Int. Ed.* **2025**, *64*, e202503117.

[28] Wang, S. S.; Zhao, Q.; Ma, Q. L.; Gan, R.; Ran, Y. L.; Fang, W. Z.; Wang, C. J.; Fang, L.; Feng, Q. G.; Zhang, Y. et al. Inducing a synergistic effect on $Pt^{\delta+}$/electron-rich sites via a platinization strategy: Generating hyper-high current density in hydrogen evolution reaction. *Nano Lett.* **2024**, *24*, 11286–11294.

[29] Qiao, L. L.; Liu, D.; Zhu, A. Q.; Feng, J. X.; Zhou, P. F.; Liu, C. F.; Ng, K. W.; Pan, H. Nickel-facilitated *in-situ* surface reconstruction on spinel Co_3O_4 for enhanced electrochemical nitrate reduction to ammonia. *Appl. Catal. B: Environ.* **2024**, *340*, 123219.

[30] Gao, P.; Zeng, Y.; Tang, P.; Wang, Z. X.; Yang, J. F.; Hu, A. P.; Liu, J. L. Understanding the synergistic effects and structural evolution of $Co(OH)_2$ and Co_3O_4 toward boosting electrochemical charge storage. *Adv. Funct. Mater.* **2022**, *32*, 2108644.

[31] Yang, X. D.; Shen, H. C.; Xiao, X. M.; Li, Z. C.; Liang, H. Q.; Chen, S.; Sun, Y. L.; Jiang, B.; Wen, G. B.; Wang, S. Y. et al. Regulating interfacial H_2O activity and H_2 bubbles by core/shell nanoarrays for 800 h stable alkaline seawater electrolysis. *Adv. Mater.* **2025**, *37*, 2416658.

[32] Ren, J. T.; Chen, L.; Wang, H. Y.; Tian, W. W.; Song, X. L.; Kong, Q. H.; Yuan, Z. Y. Synergistic activation of crystalline Ni_2P and amorphous $NiMoO_x$ for efficient water splitting at high current densities. *ACS Catal.* **2023**, *13*, 9792–9805.

[33] Zhou, L.; Sun, Y. H.; Wu, Y. S.; Zhu, Y. C.; Xu, Y. Y.; Jia, J. F.; Wang, F.; Wang, R. M. Controlled growth of Pd nanocrystals by interface interaction on monolayer MoS_2: An atom-resolved *in situ* study. *Nano Lett.* **2023**, *23*, 11360–11367.

[34] Zhao, X. R.; Zheng, H. S.; Sun, H. C.; Chen, M. P.; Wang, B. X.; Lu, Q. J.; Xiao, B.; Zhou, T.; Li, D. Q.; Qiu, G. Y. et al. Interfacial component coupling effects induce electron redistribution for enhanced hydrazine-assisted hydrogen production at ampere-level current densities. *Nano Energy* **2025**, *142*, 111201.

[35] Liu, Z.; Zeng, L. L.; Yu, J. Y.; Yang, L. J.; Zhang, J.; Zhang, X. L.; Han, F.; Zhao, L. L.; Li, X.; Liu, H. et al. Charge redistribution of Ru nanoclusters on Co_3O_4 porous nanowire via the oxygen regulation for enhanced hydrogen evolution reaction. *Nano Energy* **2021**, *85*, 105940.

[36] Cai, J. J.; Li, X. Y.; Su, B.; Guo, B. B.; Lin, X. H.; Xing, W. D.; Lu, X. F.; Wang, S. B. Rational design and fabrication of S-scheme $NiTiO_3$/CdS heterostructures for photocatalytic CO_2 reduction. *J. Mater. Sci. Technol.* **2025**, *234*, 82–89.

[37] Liu, B.; Cheng, J. Y.; Peng, H. Q.; Chen, D.; Cui, X.; Shen, D.; Zhang, K.; Jiao, T. P.; Li, M. F.; Lee, C. S. et al. *In situ* nitridated porous nanosheet networked Co_3O_4–Co_4N heteronanostructures supported on hydrophilic carbon cloth for highly efficient electrochemical hydrogen evolution. *J. Mater. Chem. A* **2019**, *7*, 775–782.

[38] Zhou, A.; Guo, X. L.; Zhong, S. Y.; Chen, Z. A.; Kang, Q. L.; Chen, M. G.; Jin, D. F.; Fan, M. Q.; Zhou, R. X.; Ma, T. L. Three birds, one-stone strategy for synthesis of hierarchically arrayed defective $MnCo_2O_4$@NF catalyst for photothermal preferential oxidation of Co in H_2-rich streams. *Chem. Eng. J.* **2023**, *471*, 144835.

[39] Teng, X. A.; Wang, Z. B.; Wu, Y. S.; Zhang, Y.; Yuan, B.; Xu, Y. Y.; Wang, R. M.; Shan, A. X. Enhanced alkaline hydrogen evolution reaction of MoO_2/Ni_3S_2 nanorod arrays by interface engineering. *Nano Energy* **2024**, *122*, 109299.

[40] Tong, K. C.; Xu, L. L.; Yao, H. X.; Wang, X. K.; Zhang, C. H.; Yang, F.; Chu, L.; Lee, J.; Jiang, H. Q.; Huang, M. H. Hydrogen spillover bridged dual nano-islands triggered by built-in electric field for efficient and robust alkaline hydrogen evolution at ampere-level current density. *Nano Res.* **2024**, *17*, 5050–5060.

[41] Kang, J. X.; Qiu, X. Y.; Hu, Q.; Zhong, J.; Gao, X.; Huang, R.; Wan, C. Z.; Liu, L. M.; Duan, X. F.; Guo, L. Valence oscillation and dynamic active sites in monolayer NiCo hydroxides for water oxidation. *Nat. Catal.* **2021**, *4*, 1050–1058.

[42] Yang, B. Q.; Wu, X. R.; Inusa, B. K.; Kuo, D. H.; Zhang, P. K.; Li, C. Z.; Liu, T.; Lu, D. F.; Yuan, Z. H.; Lin, J. G. et al. Synergistic effects of heterovalent states, oxygen vacancy defects, and surface wettability engineering in S-doped $AgBi(MoO_4)_2$ for photocatalytic hydrogen evolution. *Chem. Eng. J.* **2025**, *514*, 163151.

[43] Sheng, M. Q.; Jiang, B. B.; Wu, B.; Liao, F.; Fan, X.; Lin, H. P.; Li, Y. Y.; Lifshitz, Y.; Lee, S. T.; Shao, M. W. Approaching the volcano top: Iridium/silicon nanocomposites as efficient electrocatalysts for the hydrogen evolution reaction. *ACS Nano* **2019**, *13*, 2786–2794.

[44] Cheng, Y. F.; Lu, S. K.; Liao, F.; Liu, L. B.; Li, Y. Q.; Shao, M. W. Rh–MoS_2 nanocomposite catalysts with Pt-like activity for hydrogen evolution reaction. *Adv. Funct. Mater.* **2017**, *27*, 1700359.

[45] Shah, A. H.; Zhang, Z. S.; Wan, C. Z.; Wang, S. B.; Zhang, A.; Wang, L. Y.; Alexandrova, A. N.; Huang, Y.; Duan, X. F. Platinum surface water orientation dictates hydrogen evolution reaction kinetics in alkaline media. *J. Am. Chem. Soc.* **2024**, *146*, 9623–9630.

[46] Liu, X. B.; Wang, X. Y.; Li, K.; Tang, J. H.; Zhu, J. W.; Chi, J. Q.; Lai, J. P.; Wang, L. Diluting the resistance of built-in electric fields in oxygen vacancy-enriched Ru/$NiMoO_{4-x}$ for enhanced hydrogen spillover in alkaline seawater splitting. *Angew. Chem., Int. Ed.* **2024**, *63*, e202316319.

[47] Dai, J.; Zhu, Y. L.; Chen, Y.; Wen, X.; Long, M. C.; Wu, X. H.; Hu, Z. W.; Guan, D. Q.; Wang, X. X.; Zhou, C. et al. Hydrogen spillover in complex oxide multifunctional sites improves acidic hydrogen evolution electrocatalysis. *Nat. Commun.* **2022**, *13*, 1189.

[48] Jiang, J. Z.; Liu, S. G.; Li, Z. J.; Kim, M. G.; Jang, H.; Liu, X. E.; Hou, L. Q. Lattice-matched Ru/W_2C heterointerfaces with reversible hydrogen spillover for efficient alkaline hydrogen evolution. *Adv. Energy Mater.* **2025**, *15*, 2405546.

[49] Li, C. F.; Tian, C.; Tang, H. B.; Liu, M. R.; Zheng, L. R.; Huang, F. Z.; Li, G. R.; Li, Q. Efficient hydrogen evolution promoted by short pathway-hydrogen spillover over P-doped Pt_3Co. *ACS Energy Lett.* **2023**, *8*, 5161–5169.

[50] Lu, B. Z.; Guo, L.; Wu, F.; Peng, Y.; Lu, J. E.; Smart, T. J.; Wang, N.; Finfrock, Y. Z.; Morris, D.; Zhang, P. et al. Ruthenium atomically dispersed in carbon outperforms platinum toward hydrogen evolution in alkaline media. *Nat. Commun.* **2019**, *10*, 631.

[51] Yan, Z. T.; Tao, S.; Wang, J.; Lu, X. L.; Lu, T. B. Unlocking efficient alkaline hydrogen evolution through Ru–Sn dual metal sites and a novel hydroxyl spillover effect. *Adv. Mater.* **2024**, *36*, 2411942.

[52] Liu, G. B.; Song, C.; Li, X. L.; Jia, Q. S.; Wu, P. F.; Lou, Z. H.; Ma, Y. S.; Cui, X. J.; Zhou, X.; Jiang, L. H. Defect-rich FeCoNiMnRu high-entropy alloys with activated interfacial water for boosting alkaline water/seawater hydrogen evolution. *Chem. Eng. J.* **2025**, *509*, 161070.

[53] Ding, X.; Jiang, R.; Wu, J. L.; Xing, M. H.; Qiao, Z. L.; Zeng, X. F.; Wang, S. T.; Cao, D. P. Ni_3N–CeO_2 heterostructure bifunctional catalysts for electrochemical water splitting. *Adv. Funct. Mater.* **2023**, *33*, 2306786.

[54] Wu, J.; Wang, X.; Zheng, W. H.; Sun, Y.; Xie, Y.; Ma, K. K.; Zhang, Z.; Liao, Q. L.; Tian, Z.; Kang, Z. et al. Identifying and interpreting geometric configuration-dependent activity of spinel catalysts for water reduction. *J. Am. Chem. Soc.* **2022**, *144*, 19163–19172.

[55] Li, J. Y.; Liu, H. X.; Gou, W. Y.; Zhang, M. K.; Xia, Z. M.; Zhang, S.; Chang, C. R.; Ma, Y. Y.; Qu, Y. Q. Ethylene-glycol ligand environment facilitates highly efficient hydrogen evolution of Pt/CoP through proton concentration and hydrogen spillover. *Energy*

Environ. Sci. **2019**, *12*, 2298–2304.
[56] Jo, C.; Hwang, I.; Lee, J.; Lee, C. W.; Yoon, S. Investigation of pseudocapacitive charge-storage behavior in highly conductive ordered mesoporous tungsten oxide electrodes. *J. Phys. Chem. C* **2011**, *115*, 11880–11886.
[57] Chen, D. X.; Ding, Y. X.; Cao, X.; Wang, L. Q.; Lee, H.; Lin, G. X.; Li, W. L.; Ding, G. H.; Sun, L. C. Highly efficient biomass upgrading by a Ni–Cu electrocatalyst featuring passivation of water oxidation activity. *Angew. Chem., Int. Ed.* **2023**, *62*, e202309478.
[58] Liu, S. J.; Zhang, Z. G.; Dastafkan, K.; Shen, Y.; Zhao, C.; Wang, M. K. Yttrium-doped NiMo–MoO_2 heterostructure electrocatalysts for hydrogen production from alkaline seawater. *Nat. Commun.* **2025**, *16*, 773.
[59] Jiang, K.; Liu, Z. X.; Wang, Z.; Xie, F.; Yuan, X. Y.; Tan, Y. W. Manipulating interfacial water via metallic Pt_1Co_6 sites on self-adaptive metal phosphides to enhance water electrolysis. *Adv. Mater.* **2025**, *37*, 2419644.

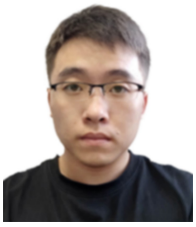

Guangxin Ren is currently a Ph.D. student in University of Science and Technology Beijing. His research focuses on nanostructured catalysts for electrochemical hydrogen evolution production and dry reforming of methane.

Aixian Shan received her Ph.D. in physics from Beihang University in 2015. After that, she worked as a postdoc at Peking University from 2015 to 2017. Currently, she is an associate professor at the University of Science and Technology Beijing. She has been focusing her research on design, synthesis, characterization, and interface modulation for electro-catalysts applied in H_2 production and fuel cells.

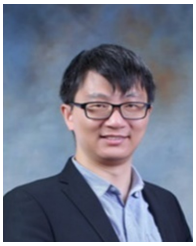

Yingying Xu received his Bachelor's degree in Physics and his Ph.D. in Condensed Matter Physics from the School of Physics at Peking University. Currently, he serves as an associate professor in the School of Mathematics and Physics at the University of Science and Technology Beijing. His primary research focuses on the atomic-scale simulation of surface and interface material systems. A significant part of his recent work involves investigating catalyst performance and surface reconstruction phenomena in transition metal materials for energy-related applications.

Rongming Wang is a Professor at the University of Science and Technology Beijing (China) and a Leading Scholar of USTB, as well as a recipient of the National "Hundred, Thousand and Ten Thousand Talents Project." His research centers on advanced material interface engineering, quantitative and *in situ* transmission electron microscopy, atomic-scale microstructural characterization, and atomic-level manufacturing. He has developed quantitative electron microscopy approaches for crystal interface and lattice strain analysis, pioneered atomic-resolution *in situ* dynamic characterization techniques, and advanced process-oriented growth pathway control in atomic manufacturing. His work enables the precise construction and performance optimization of functional materials and nanodevices for applications in energy, catalysis, and information technology. He has published over 300 SCI-indexed papers in leading journals, including *Nature*, *Science*, *Physical Review Letters*, and *Advanced Materials*, with more than 18,000 citations (H-index 70).